

Title: Observation of a three-dimensional fractional Hall response in HfTe₅

Authors: S. Galeski^{1#}, X. Zhao^{2,3,4}, R. Wawrzyńczak¹, T. Meng⁵, T. Förster⁶, S. Honnali¹, N. Lamba¹, T. Ehmcke⁵, A. Markou¹, W. Zhu^{2,4}, J. Wosnitza^{6,7}, C. Felser¹, G. F. Chen^{2,3,4}, J. Gooth^{1,7*}

Affiliations:

¹Max Planck Institute for Chemical Physics of Solids, Nöthnitzer Straße 40, 01187 Dresden, Germany.

²Institute of Physics and Beijing National Laboratory for Condensed Matter Physics, Chinese Academy of Sciences, Beijing 100190, China.

³Songshan Lake Materials Laboratory, Dongguan, Guangdong 523808, China.

⁴School of Physics Science, University of Chinese Academy of Sciences, Beijing 100049, China.

⁵Institute of Theoretical Physics, Technische Universität Dresden, 01062 Dresden, Germany.

⁶Hochfeld-Magnetlabor Dresden (HLD-EMFL) and Würzburg-Dresden Cluster of Excellence ct.qmat, Helmholtz-Zentrum Dresden-Rossendorf, 01328 Dresden, Germany.

⁷Institut für Festkörper- und Materialphysik, Technische Universität Dresden, 01062 Dresden, Germany.

#stanislaw.galeski@cpfs.mpg.de, *johannes.gooth@cpfs.mpg.de

Abstract:

Interacting electrons in two dimensions can bind magnetic flux lines to form composite quasiparticles with fractional electric charge, manifesting themselves in the fractional quantum Hall effect (FQHE). Although the FQHE has also been predicted to occur in three dimensions, it has not yet been experimentally observed. Here, we report the observation of fractional plateaus in the Hall conductivity of the bulk semimetal HfTe₅ at magnetic fields beyond the quantum limit. The plateaus are accompanied by Shubnikov-de Haas minima of the longitudinal electrical resistivity. The height of the Hall plateaus is given by twice the Fermi wave vector in the direction of the applied magnetic field and scales with integer and particular fractional multiples of the conductance quantum. Our findings are consistent with strong electron-electron interactions, stabilizing a fractionalized variant of the Hall effect in three dimensions.

Main Text:

The quantum Hall effect (QHE) is the quantization of the Hall conductivity σ_{xy} in two-dimensional (2D) electron systems (2DESSs) to values of ve^2/h , where e is the electron charge, h the Planck constant and ν is the filling factor – the number of electrons per magnetic flux quanta. In the case of non-interacting electrons, ν takes only integer values.(1) However, once interactions between the electrons become important, ν can also take fractional values.(2)

Depending on whether ν is an integer or a fraction, the QHE is referred to as the integer (IQHE) or fractional quantum Hall effect (FQHE), respectively.

In isotropic three-dimensional (3D) systems, the electron motion along the third direction usually leads to a gapless band structure, which in turn destroys the quantization of the Hall effect.(3–5) However, it has been predicted that a generalized version of the QHE can emerge in 3D electron systems that exhibit a periodically modulated superstructure, provided the chemical potential resides in the associated density wave gap.(6–8) The Hall conductivity σ_{xy} is then quantized in values of $\nu e^2/h \cdot G_z/2\pi$, where G_z is the wave vector of the superstructure along the magnetic field. Such a system can be viewed as a 3D stack of (integer) quantum Hall layers of filling factor ν with an inter-layer distance of $\lambda_z = 2\pi/G_z$. In the presence of strong electron-electron interactions, stacked versions of fractional quantum Hall effects have also been predicted, which reveal themselves in fractional Hall responses.(3, 9–12)

Inspired by these ideas, the 3D QHE has been explored in several material systems. For example, signatures of the IQHE have been found in quasi-2D semiconducting multilayer lattices,(13) Bechgaards salts,(14, 15) η -Mo₄O₁₁,(16) n -doped Bi₂Te₃,(17) and EuMnBi₂,(18) in which the layered crystal structure itself supplies the stack of 2D systems. Very recently, the IQHE has also been observed in 3D graphite films(5) and bulk ZrTe₅ samples.(19) In graphite, the imposed periodic superstructure has been attributed to the formation of standing electron waves; in ZrTe₅, however, the superstructure is believed to arise from a charge density wave (CDW), because its propagation vector turned out to be $G_z = 2k_{F,z}$. Likewise, there has been a long-standing experimental effort to observe fractional quantum Hall states in three-dimensions. However, apart from signatures of fractionalization in the longitudinal electrical resistivity of Bi(20, 21), ZrTe₅(19, 22) and graphite,(5) the observation of the 3D FQHE is so far elusive.

In this work, we have investigated the low-temperature magneto-transport properties of the 3D semimetal HfTe₅. Previous studies have shown that HfTe₅ is an isostructural counterpart of ZrTe₅.(23) Both materials share an orthorhombic crystal structure and a single elliptical 3D Fermi surface, comprising less than 1% of the Brillouin zone and hosting massive Dirac fermions with almost linearly dispersing bands in the vicinity of the Fermi level (see Supplementary Materials for details). In ZrTe₅, these specific properties have been considered essential for the observation of the 3D IQHE.(19) In particular, the associated low electron density and anisotropic crystal structure are believed to enhance e-e interactions and thus to favor the formation of a CDW – arguments that apply to HfTe₅ alike. In addition, hafnium has a higher atomic number than zirconium and hence naturally introduces stronger spin-orbit coupling,(23) which has been shown to stabilize fractional quantum Hall states in 2DESs.(24) Moreover, recent progress in HfTe₅ single-crystal growth has achieved charge mobility μ that exceeds 200,000 cm²V⁻¹s⁻¹ at low temperatures (< 4 K) (see Methods for details). The quality of these crystals is comparable to that of graphene samples, which have previously proven appropriate for observing the FQHE in two dimensions.(25) Therefore, HfTe₅ is an ideal candidate for the observation of fractional Hall responses in 3D.

HfTe₅ typically grows as millimeter-long ribbons with an aspect ratio of approximately 1:3:10, reflecting its crystalline anisotropy. Details of the growth process, crystal structure and first transport characterization of our samples can be found in Ref. (26). We have measured the longitudinal electrical resistivity ρ_{xx} and Hall resistivity ρ_{xy} of three HfTe₅ samples (A, B, C) as a function of magnetic field \mathbf{B} and temperature T , with the electrical current applied along the a -axis of the crystals.

At $T = 300$ K, ρ_{xx} is around 0.5 m Ω cm (see Fig.1A, Fig. S1 and Ref. (26)) with an electron density of $n = 1.3 \times 10^{19}$ cm $^{-3}$ and $\mu = 10,000$ cm 2 V $^{-1}$ s $^{-1}$.(26) Upon cooling at zero magnetic field, ρ_{xx} increases with decreasing T until it reaches a maximum at $T_L = 70$ K (Fig.1A). This maximum has previously been observed in HfTe $_5$ (26) and ZrTe $_5$,(19) and attributed to a Lifshitz transition, that is a change in charge-carrier type. Consistently, the slope of $\rho_{xy}(\mathbf{B})$ changes sign at T_L , indicating electron-type transport for $T < T_L$.(26). At 3 K, we find $n = 8.7 \times 10^{16}$ cm $^{-3}$ and $\mu = 250,000$ cm 2 V $^{-1}$ s $^{-1}$ (see Materials and Methods and Fig. S2). All investigated samples show similar electrical transport properties. The data presented in the main text was obtained from sample A. Additional data of samples B and C can be found in the Supplementary Materials.

To characterize the Fermi surface (FS) morphology of our HfTe $_5$ samples, we have measured Shubnikov-de Haas (SdH) oscillations with respect to the main crystal axes at 3 K. For this purpose, we followed the analysis of Ref. (19) and rotated \mathbf{B} in the z - y and z - x planes, while measuring $\rho_{xx}(\mathbf{B})$ at a series of different angles (Fig. 1 and Fig. S3). The SdH frequency $B_{F,i}$ is directly related to the extremal cross-section of the Fermi surface $S_{F,i}$, normal to the applied \mathbf{B} direction *via* the Onsager relation $B_{F,i} = S_{F,i}(\hbar/2\pi e)$. Examples of the SdH oscillations for which the magnetic field was aligned along the three principal crystallographic directions (x , y and z axes) are shown in Fig. 1B, C and D (upper panels). In each field direction, we have observed maxima in ρ_{xx} that are periodic in $1/B$, each of which corresponds to the onset of a Landau level (LL). In the associated minima, $\rho_{xx}(\mathbf{B})$ does not vanish, which is a consequence of the remaining dispersion in z -direction in 3D systems and LL-broadening due to disorder (see Materials and Methods and Fig. S4-S7 for details). To determine the SdH oscillation frequency, we have subtracted the smooth high-temperature (50K) - $\rho_{xx}(\mathbf{B})$ from the low- T -data, obtaining the oscillating part of the longitudinal resistivity $\Delta\rho_{xx}(\mathbf{B})$. Employing a standard Landau-index fan diagram analysis to $\Delta\rho_{xx}(\mathbf{B})$ (Fig. 1H, Fig. S3, Fig. S8, Fig. S9 and Materials and Methods), we have found only a single oscillation frequency for all rotation angles measured, consistent with a single electron pocket at the Fermi energy. The extracted $B_{F,i}$ of sample A for \mathbf{B} along the three principal directions are $B_{F,x} = (9.9 \pm 0.1)$ T, $B_{F,y} = (14.5 \pm 0.5)$ T, and $B_{F,z} = (1.3 \pm 0.1)$ T. Here, the errors denote the standard deviation of the corresponding fits.

In contrast to 2D materials, HfTe $_5$ shows in-plane SdH oscillations when \mathbf{B} is aligned with x and y , indicating a 3D Fermi-surface pocket. The shape of the FS is further determined by the analysis of the rotation angle-dependence of B_F . As shown in Fig. 1I and J, the angle-dependent SdH frequency is well represented by a 3D ellipsoidal equation $B_{F,3D} = B_{F,z}B_{F,i} / \sqrt{(B_{F,z} \sin \theta)^2 + (B_{F,i} \cos \theta)^2}$, where θ is the rotation angle in the z - i plane. As a cross-check, we also plot the formula of a 2D cylindrical Fermi surface $B_{F,2D} = B_{F,z} / \cos \theta$, which deviates significantly from the experimental data for $\theta > 80^\circ$. Hence the ellipsoid equations can be used to obtain the Fermi wave vectors $k_{F,x} = \sqrt{S_{F,y}S_{F,z}} / \sqrt{\pi S_{F,x}} = (0.005 \pm 0.001)$ \AA^{-1} , $k_{F,y} = \sqrt{S_{F,x}S_{F,z}} / \sqrt{\pi S_{F,y}} = (0.008 \pm 0.001)$ \AA^{-1} and $k_{F,z} = \sqrt{S_{F,x}S_{F,y}} / \sqrt{\pi S_{F,z}} = (0.058 \pm 0.006)$ \AA^{-1} that span the 3D FS of HfTe $_5$ in the x , y , and z direction, respectively (Fig. 1K). The errors in $k_{F,i}$ originate from the errors of the $B_{F,i}$. The preceding analysis indicates that for our HfTe $_5$ samples, the quantum limit with the field along the z is achieved already for the field of 1.8 T. Further details of our band-structure analysis can be found in Fig.S6 and Table S1.

For the field aligned with the z -axis ($\mathbf{B} \parallel z$), we additionally observed pronounced plateaus in Hall resistance $\rho_{xy}(\mathbf{B})$ that appear at the minima of the SdH oscillations in $\rho_{xx}(\mathbf{B})$ —features commonly related to the QHE (Fig 2A). Similar to ZrTe $_5$,(19) the height of the plateaus is given by $1/\nu$ (\hbar/e^2) $\pi/k_{F,z}$ with approximately integer ν . The plateaus are most pronounced at low temperatures, but still visible up to $T = 30$ K (Fig. 2B and C). We note that the observed

quantization of ρ_{xy} is not immediately obvious from the predicted quantization in σ_{xy} . The Hall resistivity tensor is given by $\rho_{xy} = \sigma_{xy}/(\sigma_{xx}^2 + \sigma_{xy}^2)$, where σ_{xx} is the longitudinal component of the conductivity tensor. However, in our samples at low temperatures $\sigma_{xx} < \sigma_{xy}$ (Fig. S11 and Fig. S12) and thus $\sigma_{xy}^{-1} \approx \rho_{xy}$, enabling the direct observation of the quantization.

Fig. 2D shows the angular-dependence of the Hall plateaus, which we find to scale with the rotation angle as in ZrTe₅.⁽¹⁹⁾ In both materials, the height of the Hall plateaus and its position in $|\mathbf{B}|$ depends only on the field component that is perpendicular to the x - y plane $B_{\perp} = |\mathbf{B}|\cos\theta$. These are typical signatures for a 3D IQHE within a periodical superlattice.

Similarly to the case of ZrTe₅,⁽¹⁹⁾ the superlattice modulation has the period $\lambda_z = 2\pi/G_z$, equal to half of the Fermi wavelength $\lambda_F/2 = \pi/k_{F,z} \approx 11$ nm. This length scale is an order of magnitude larger than the lattice constant of HfTe₅ along z (about 1.4 nm),⁽²³⁾ suggesting that the observed IQHE has an electronic origin. As explained above, for ZrTe₅,⁽¹⁹⁾ it was argued that such an electronic superlattice arises from the formation of a CDW.

Above 6 T, we find that $\rho_{xx}(\mathbf{B})$ steeply increases with magnetic field (Fig. 2B). Such a steep increase has previously been observed in ZrTe₅ as well and has been attributed to a field-induced metal-insulator transition.⁽¹⁹⁾

So far, our analysis focused on similarities between the IQHEs observed in ZrTe₅ and HfTe₅. Upon cooling our HfTe₅ samples down to 50 mK, obvious differences begin to emerge, as shown in Fig. 3A. In addition to maxima in $\rho_{xx}(\mathbf{B})$ (left axes) and quantized Hall plateaus in $\rho_{xy}(\mathbf{B})$ (right axes) at integer fillings factors for $\mathbf{B} \parallel z$, a maximum in $\rho_{xx}(\mathbf{B})$ at $\nu = 6/5$ (upper panel) and a more pronounced maximum at $\nu = 3/5$ (lower panel) appear. The filling factors of the additional maxima are identified using the Landau index fan diagram obtained with the integer fillings at 3 K. Each of these fillings is confirmed by corresponding oscillations in $\rho_{xx}(\mathbf{B})$ of all three samples investigated (compare Fig. S11 and Fig. S12), despite the fractional states being less pronounced in some of them. However, even in the cleanest sample, the corresponding Hall plateaus do not exhibit exact quantization. The weak formation of the fractional Hall plateaus in $\rho_{xy}(\mathbf{B})$ may be related to the proximity of the $\nu = 1$ and $\nu = 6/5$ states and the presence of the insulating phase close to the $\nu = 3/5$ state at high magnetic fields, leading to competing features in ρ_{xx} . To perform a more direct comparison to theory we have calculated $\sigma_{xy}(\mathbf{B})$. The results shown in Fig. 3B (right axes) are consistent with a 3D FQHE. The quantization of $\sigma_{xy}(\mathbf{B})$ to values of $\nu \cdot e^2/h \cdot k_{F,z}/\pi$ is found to be within 8% and 2% (see Supplementary Materials for details) of the values expected for filling factors $\nu = 6/5$ (upper panel) and at $\nu = 3/5$ (lower panel), respectively.

A characteristic of QHE systems with $\mathbf{B} \parallel z$ is that the line shape of $\Delta\rho_{xx}(\mathbf{B})$ looks very much like the line shape of $\sigma_{xx}(\mathbf{B})$.⁽²⁷⁾ In addition, it was shown that dissipation in both integer and fractional QHE systems is related to local variation of $\rho_{yx}(\mathbf{B})$ and connects to $\rho_{xx}(\mathbf{B})$ as $\rho_{xx}(B_z) = \gamma \mathbf{B} \cdot d\rho_{yx}(\mathbf{B})/d\mathbf{B}$, where γ is a dimensionless parameter of the order of 0.01-0.05, which measures the local electron concentration fluctuations.^(28, 29) To test these relations for the 3D Hall effect in HfTe₅, we have plotted $\sigma_{xx}(\mathbf{B})$ (Fig. 3D) and $\gamma \mathbf{B} \cdot d\rho_{yx}(\mathbf{B})/d\mathbf{B}$, (Fig. 3E, upper panel) as a function of B^{-1} and find that both quantities show maxima and minima at the same field positions as $\Delta\rho_{xx}(\mathbf{B})$. In particular, the derivative relation is well fulfilled with $\gamma = 0.04$, which is in the expected range reported for 2DESs. These results indicate that the integer and fractional plateaus observed in $\sigma_{xy}(\mathbf{B})$ of HfTe₅, are indeed related to quantum Hall physics.

To gain further insights into the 3D Hall effect in HfTe₅, we estimate the gap energies Δ_{ν} associated with the integer and fractional plateaus from the T -dependence of the $\rho_{xx}(\mathbf{B})$ minima

(Fig. 3F) in the thermally activated regime $\rho_{xx}(\mathbf{B}) \propto \exp(\Delta_\nu/2k_B T)$, where k_B is the Boltzmann constant (Fig. S13). For integer ν , we find $\Delta_1 = (40 \pm 2)$ K at $\nu = 1$ and $\Delta_2 = (9 \pm 1)$ K at $\nu = 2$. The gap energies of the fractional plateaus are two orders of magnitude lower: for the $\nu = 3/5$ state, we estimate $\Delta_{3/5} = (0.49 \pm 0.09)$ K and $\Delta_{6/5} = (0.27 \pm 0.06)$ K for the $\nu = 6/5$ state. The deviations given for the gaps are the errors obtained from the fits in Fig. S13. In spite of considerable LL broadening, both the size of the gaps of the integer and fractional plateaus compare well with the gaps obtained in 2DESs.(27, 30) The different Δ_ν are also in agreement with the T -dependence of the corresponding Hall plateaus (Fig. 3G). While the integer plateaus are observable up to tens of Kelvin, the fractional ones vanish at around 0.5 K.

Based on magneto-transport measurements up to 70 T (Fig. S14), we exclude the presence of additional bands at the Fermi level. Our data must, therefore, be analysed in terms of a single electronic Dirac pocket. At fields below the quantum limit of $B_z = 1.8$ T, multiple spinful Landau level bands may be present at the Fermi level. While more intricate explanations are possible, we thus cannot exclude the fractional value of the Hall conductivity at $\nu = 6/5$ to result from multiband effects. The observed fractional value of σ_{xy} might for example result from a Zeeman splitting of the first Landau level.

For the fractional Hall plateau at $\nu = 3/5$, the situation is markedly different. This plateau arises well above the quantum limit. It is thus associated with physics in the zeroth Landau level only (this Landau level is non-degenerate since HfTe₅ is a gapped Dirac semimetal). The finite value of ρ_{xx} at $\nu = 3/5$ implies the absence of a fully established bulk gap (possibly due to thermally activated carriers as explained above), which in turn means that a truly quantized Hall effect cannot be expected. Nevertheless, the emergence of the $\nu = 3/5$ -plateau in a single-band system at low temperatures calls for an explanation beyond a simple single-particle picture: The Hall conductivity of a non-interacting single band in which the chemical potential adjusts to keep the particle number fixed simply decreases as $1/B$.

At low temperatures and high fields, a layered structure along the z -direction can arise independently of a possibly present low-field density wave. As proposed based on a Hartree-Fock analysis,(9) a gain in exchange energy can exceed the energy cost for distributing electrons unequally between layers. The electrons then undergo spontaneous staging transitions in which only every N -th layers is occupied, while all other layers are emptied (the number N depends on the average electron density and the state formed). Depending on layer separation, electron density, and the strength of electron-electron interactions, various types of layered Laughlin states or Halperin states can then be formed.(3, 9, 12) These states are naturally associated with fractional Hall responses. While staging transitions are unlikely in isotropic three-dimensional materials at high electron densities, HfTe₅ has a very anisotropic band structure with small tunnelling amplitudes along z , and hosts only a relatively small number of electrons in its Dirac pocket. Our data is thus consistent with strong interactions stabilizing a fractional Hall response in HfTe₅ at fields beyond the quantum limit.

In conclusion, our measurements reveal plateaus in $\sigma_{xy}(\mathbf{B})$ of the bulk semimetal HfTe₅, accompanied by SdH minima in $\rho_{xx}(\mathbf{B})$. The height of the Hall plateaus is given by twice $k_{F,z}$ in the direction of the applied magnetic field and scales with integer and particular fractional multiples of the conductance quantum – signatures that are suggestive of a fractional Hall effect in a 3D crystal. However, further experimental and theoretical efforts in determining the real interactions and texture of the Hall effect in HfTe₅ are necessary to settle the puzzle of the $\nu = 3/5$ -plateau.

References:

1. K. V. Klitzing, G. Dorda, M. Pepper, New method for high-accuracy determination of the fine-structure constant based on quantized hall resistance. *Phys. Rev. Lett.* **45**, 494–497 (1980).
2. D. C. Tsui, H. L. Stormer, A. C. Gossard, Two-dimensional magnetotransport in the extreme quantum limit. *Phys. Rev. Lett.* **48**, 1559 (1982).
3. F. J. Burnell, B. A. Bernevig, D. P. Arovas, Scenario for fractional quantum Hall effect in bulk isotropic materials. *Phys. Rev. B.* **79**, 155310 (2009).
4. J. T. Chalker, in *Supersymmetry and Trace Formulae* (Springer, 1999), pp. 75–83.
5. J. Yin, S. Slizovskiy, Y. Cao, S. Hu, Y. Yang, I. Lobanova, B. A. Piot, S.-K. Son, S. Ozdemir, T. Taniguchi, K. Watanabe, K. S. Novoselov, F. Guinea, A. K. Geim, V. Fal’ko, A. Mishchenko, Dimensional reduction, quantum Hall effect and layer parity in graphite films. *Nat. Phys.* **15**, 437–442 (2019).
6. B. I. Halperin, Possible states for a three-dimensional electron gas in a strong magnetic field. *Jpn. J. Appl. Phys.* **26**, 1913 (1987).
7. M. Kohmoto, B. I. Halperin, Y.-S. Wu, Diophantine equation for the three-dimensional quantum Hall effect. *Phys. Rev. B.* **45**, 13488 (1992).
8. B. A. Bernevig, T. L. Hughes, S. Raghu, D. P. Arovas, Theory of the three-dimensional quantum Hall effect in graphite. *Phys. Rev. Lett.* **99**, 146804 (2007).
9. A. H. MacDonald, Staging transitions in multiple-quantum-well systems. *Phys. Rev. B.* **37**, 4792 (1988).
10. J. D. Naud, L. P. Pryadko, S. L. Sondhi, Notes on infinite layer quantum Hall systems. *Nucl. Phys. B.* **594**, 713–746 (2001).
11. C. B. Hanna, J. C. Diaz-Velez, A. H. MacDonald, Broken-symmetry states in quantum Hall superlattices. *Phys. Rev. B.* **65**, 115323 (2002).
12. X. Qiu, R. Joynt, A. H. MacDonald, Phase transitions in a multiple quantum well in strong magnetic fields. *Phys. Rev. B.* **42**, 1339 (1990).
13. H. L. Störmer, J. P. Eisenstein, A. C. Gossard, W. Wiegmann, K. Baldwin, Quantization of the Hall effect in an anisotropic three-dimensional electronic system. *Phys. Rev. Lett.* **56**, 85 (1986).
14. S. T. Hannahs, J. S. Brooks, W. Kang, L. Y. Chiang, P. M. Chaikin, Quantum Hall effect in a bulk crystal. *Phys. Rev. Lett.* **63**, 1988 (1989).
15. J. R. Cooper, W. Kang, P. Auban, G. Montambaux, D. Jérôme, K. Bechgaard, Quantized Hall effect and a new field-induced phase transition in the organic superconductor (TMTSF) 2 PF 6. *Phys. Rev. Lett.* **63**, 1984 (1989).
16. S. Hill, S. Uji, M. Takashita, C. Terakura, T. Terashima, H. Aoki, J. S. Brooks, Z. Fisk, J. Sarrao, Bulk quantum Hall effect in η -Mo₄O₁₁. *Phys. Rev. B.* **58**, 10778 (1998).
17. H. Cao, J. Tian, I. Miotkowski, T. Shen, J. Hu, S. Qiao, Y. P. Chen, Quantized Hall effect and Shubnikov–de Haas oscillations in highly doped Bi₂Se₃: Evidence for layered transport of bulk carriers. *Phys. Rev. Lett.* **108**, 216803 (2012).

18. H. Masuda, H. Sakai, M. Tokunaga, Y. Yamasaki, A. Miyake, J. Shiogai, S. Nakamura, S. Awaji, A. Tsukazaki, H. Nakao, Quantum Hall effect in a bulk antiferromagnet EuMnBi_2 with magnetically confined two-dimensional Dirac fermions. *Sci. Adv.* **2**, e1501117 (2016).
19. F. Tang, Y. Ren, P. Wang, R. Zhong, J. Schneeloch, S. A. Yang, K. Yang, P. A. Lee, G. Gu, Z. Qiao, L. Zhang, Three-dimensional quantum Hall effect and metal–insulator transition in ZrTe_5 . *Nature*. **569**, 537–541 (2019).
20. H. Yang, B. Fauque, L. Malone, A. B. Antunes, Z. Zhu, C. Uher, K. Behnia, Phase diagram of bismuth in the extreme quantum limit. *Nat. Commun.* **1**, 47 (2010).
21. K. Behnia, L. Balicas, Y. Kopelevich, Signatures of electron fractionalization in ultraquantum bismuth. *Science* **317**, 1729–1731 (2007).
22. W. Yu, Y. Jiang, J. Yang, Z. L. Dun, H. D. Zhou, Z. Jiang, P. Lu, W. Pan, Quantum oscillations at integer and fractional Landau level indices in single-crystalline ZrTe_5 . *Sci. Rep.* **6**, 35357 (2016).
23. H. Weng, X. Dai, Z. Fang, Transition-metal pentatelluride ZrTe_5 and HfTe_5 : A paradigm for large-gap quantum spin Hall insulators. *Phys. Rev. X*. **4**, 11002 (2014).
24. T. Ito, K. Nomura, N. Shibata, Spin–Orbit Interaction Enhanced Fractional Quantum Hall States in the Second Landau Level. *J. Phys. Soc. Japan*. **79**, 73003 (2010).
25. K. I. Bolotin, F. Ghahari, M. D. Shulman, H. L. Stormer, P. Kim, Observation of the fractional quantum Hall effect in graphene. *Nature*. **462**, 196 (2009).
26. L.-X. Zhao, X.-C. Huang, Y.-J. Long, D. Chen, H. Liang, Z.-H. Yang, M.-Q. Xue, Z.-A. Ren, H.-M. Weng, Z. Fang, Anomalous magneto-transport behavior in transition metal pentatelluride HfTe_5 . *Chinese Phys. Lett.* **34**, 37102 (2017).
27. C. R. Dean, A. F. Young, P. Cadden-Zimansky, L. Wang, H. Ren, K. Watanabe, T. Taniguchi, P. Kim, J. Hone, K. L. Shepard, Multicomponent fractional quantum Hall effect in graphene. *Nat. Phys.* **7**, 693 (2011).
28. A. M. Chang, D. C. Tsui, Experimental observation of a striking similarity between quantum Hall transport coefficients. *Solid State Commun.* **56**, 153–154 (1985).
29. S. H. Simon, B. I. Halperin, Explanation for the resistivity law in quantum Hall systems. *Phys. Rev. Lett.* **73**, 3278 (1994).
30. R. G. Clark, J. R. Mallett, S. R. Haynes, J. J. Harris, C. T. Foxon, Experimental determination of fractional charge e/q for quasiparticle excitations in the fractional quantum Hall effect. *Phys. Rev. Lett.* **60**, 1747 (1988).

Notes:

The authors declare no competing financial interests.

Author contributions

S.G and J.G. conceived the experiment. X.Z., W.Z. and G.F.C. synthesized the single-crystal HfTe₅ bulk samples. S.G., and S.H. fabricated the electrical transport devices. A.M. and C.F. sputtered the electrical contacts on the samples. S.G. carried out the low-field transport measurements with the help of S.H., J.G. and R.W.. S.G., J.G., T.F. and J.W. carried out the high-field transport experiments. T.E. and T.M. provided the model of the three-dimensional quantum Hall effect. S.G., N.L., T.M., T.F. and J.G. analyzed the data. All authors contributed to the interpretation of the data and to the writing of the manuscript.

Acknowledgments:

The authors thank Andrei Bernevig for fruitful discussions. T.M. acknowledges funding by the Deutsche Forschungsgemeinschaft via the Emmy Noether Programme ME4844/1- 1, the Collaborative Research Center SFB 1143, project A04, and the Cluster of Excellence on Complexity and Topology in Quantum Matter *ct.qmat* (EXC 2147). C.F. acknowledges the research grant DFG-RSF (NI616 22/1): Contribution of topological states to the thermoelectric properties of Weyl semimetals and SFB 1143. G. F. C. was supported by the Ministry of Science and Technology of China through Grant No. 2016YFA0300604, and the National Natural Science Foundation of China through Grant No. 11874417. T.F. and J.W. acknowledge support from the DFG through the Würzburg-Dresden Cluster of Excellence on Complexity and Topology in Quantum Matter *ct.qmat* (EXC 2147, project-id 39085490), the ANR-DFG grant Fermi-NESt, and by Hochfeld-Magnetlabor Dresden (HLD) at HZDR, member of the European Magnetic Field Laboratory (EMFL). J.G. acknowledges support from the European Union's Horizon 2020 research and innovation program under Grant Agreement ID 829044 "SCHINES".

Supplementary materials:

Materials and Methods

Fig. S1 – S14

Table S1

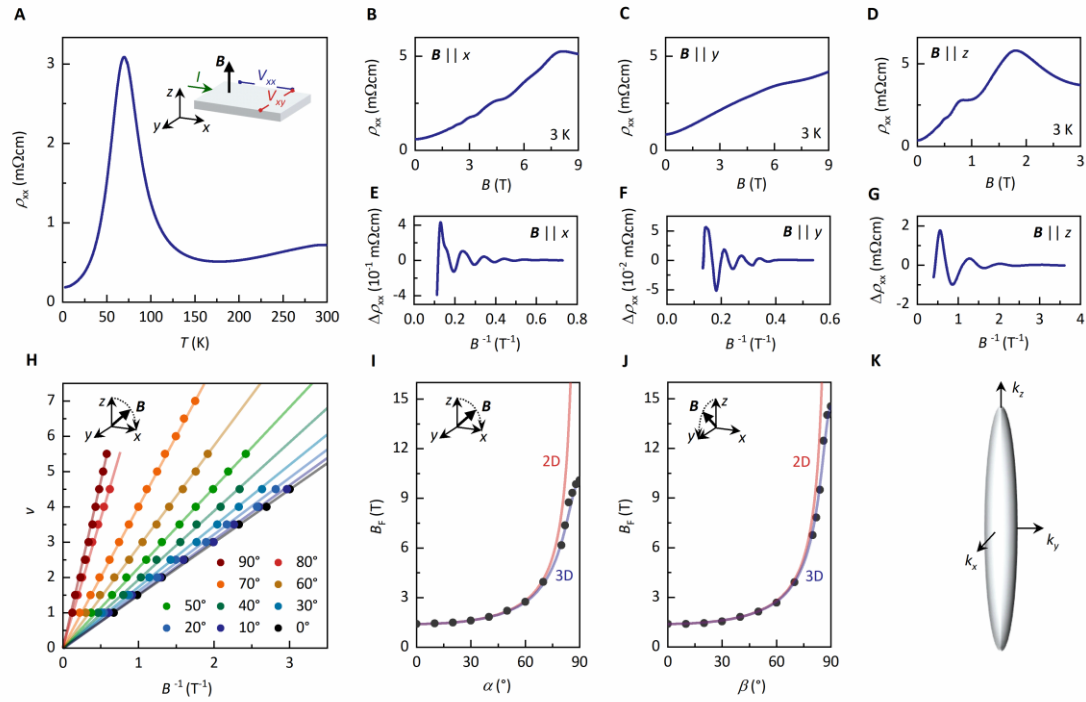


Fig. 1. Three-dimensional morphology of the Fermi surface in HfTe₅. (A) Longitudinal electrical resistivity ρ_{xx} as a function of temperature T at zero magnetic field. Inset: Sketch of the measurement configuration in the three spatial directions x , y , and z . The bias current I is applied along x and the magnetic field \mathbf{B} along z . The corresponding voltage responses are measured in x - (V_{xx}) and in y -direction (V_{xy}). (B) ρ_{xx} as a function of \mathbf{B} at 3 K with \mathbf{B} applied along x , (C) along y and (D) along the z -direction. (E) Variation of the longitudinal electrical resistivity $\Delta\rho_{xx}$ as a function of \mathbf{B} at 3 K with \mathbf{B} applied along x , (F) along y , and (G) along the z -direction. (H), Landau index fan diagram for the integer filling factors ν for different angles α of \mathbf{B} in the z - x plane (see inset; α is positive from the z to the x direction) as a function of \mathbf{B}^{-1} . The data is obtained from the minima of ρ_{xx} in Extended data Fig. 3A. (I) Shubnikov-de Haas frequency as a function of angle α and (J) β . β is the rotation angle of \mathbf{B} in the z - y plane (see inset; β is positive from the z to the y direction). The black dots represent the measurement data. The red fitting curve represents a quasi-2D Fermi surface, the blue fitting curve corresponds to an ellipsoidal 3D Fermi surface. (K) The Fermi surface of HfTe₅ in momentum space along the k_x , k_y and k_z direction.

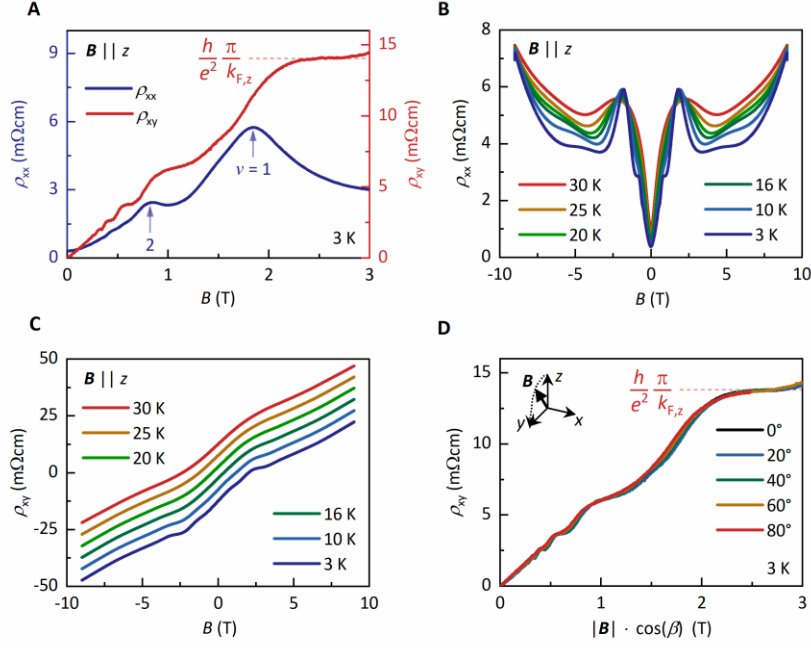


Fig. 2. Three-dimensional integer quantum Hall effect in HfTds. (A) Longitudinal electrical resistivity ρ_{xx} (blue, left axis) and Hall resistivity ρ_{xy} (red, right axis) and as a function of \mathbf{B} at $T = 3$ K with \mathbf{B} applied in z . The blue arrows mark the onset of a Landau level (LL). The blue numbers denote the filling factor ν of the corresponding LL. The plateaus in ρ_{xy} scale with $1/\nu$ $(h/e^2) \pi/k_{F,z}$, with the Planck constant h , the electron charge e , and the Fermi wave vector in z -direction $k_{F,z}$. (B) ρ_{xx} and (C) ρ_{xy} as a function of \mathbf{B} for various temperatures $T \geq 3$ K with \mathbf{B} applied in z . (D) ρ_{xy} as a function of $|\mathbf{B}|/\cos(\beta)$ for magnetic fields along direction with angles β at 3 K.

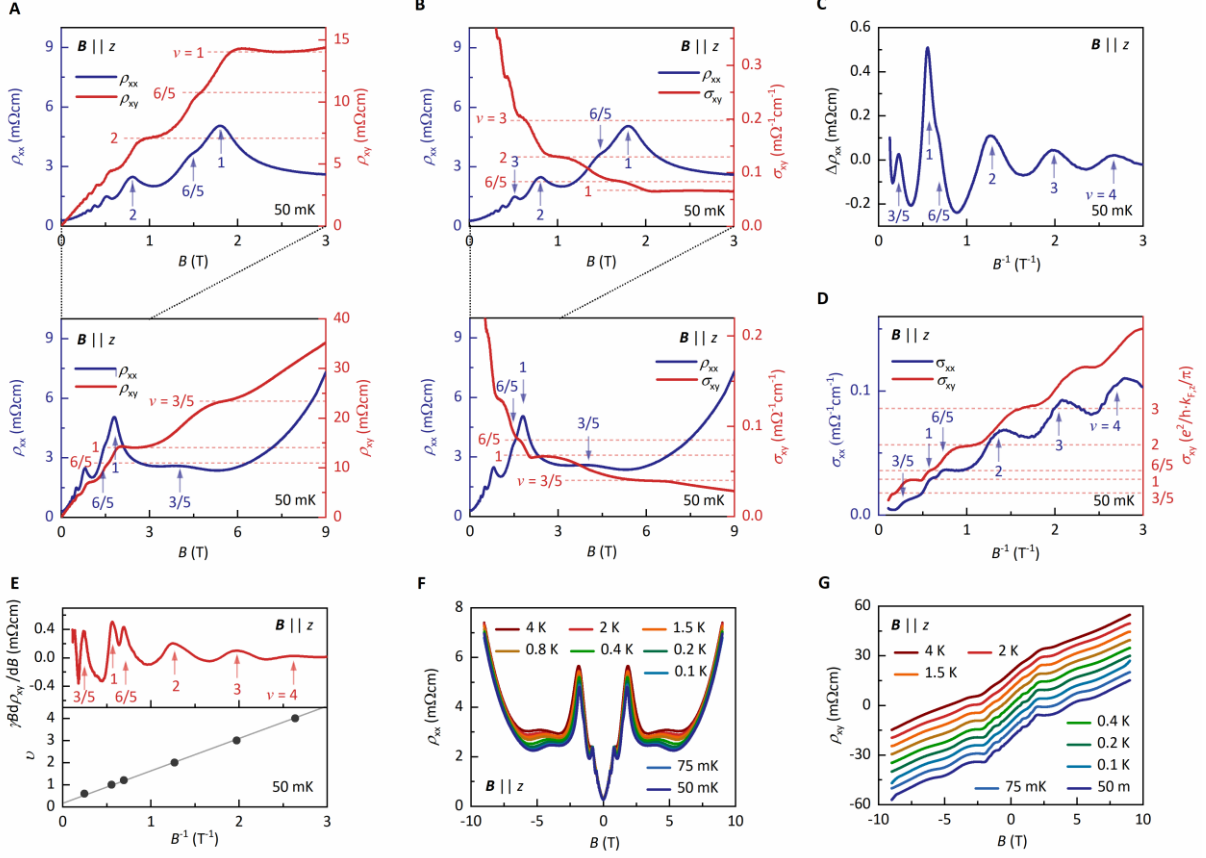


Fig. 3. Three-dimensional fractional quantum Hall effect in HfTe₅. (A) Longitudinal electrical resistivity ρ_{xx} (blue, left axis) and Hall resistivity ρ_{xy} (red, right axis) as a function of B at $T = 50$ mK with B applied in z for $0 \text{ T} \leq B \leq 3 \text{ T}$ (upper panel) and $0 \text{ T} \leq B \leq 9 \text{ T}$ (lower panel). The blue arrows mark the onset of a Landau level (LL). The blue and red numbers label the filling factor ν of the corresponding LL. (B) Longitudinal electrical resistivity ρ_{xx} (blue, left axis) and Hall conductivity σ_{xy} (red, right axis) as a function of B at $T = 50$ mK with B applied in z for $0 \text{ T} \leq B \leq 3 \text{ T}$ (upper panel) and $0 \text{ T} \leq B \leq 9 \text{ T}$ (lower panel). (C) Variation of the longitudinal electrical resistivity $\Delta\rho_{xx}$ as a function of B at 50 mK with B applied along z . (D) Longitudinal electrical conductivity σ_{xx} (blue, left axis) and Hall conductivity σ_{xy} (red, right axis) as a function of B^{-1} at $T = 50$ mK with B applied in z . (E) $\gamma \cdot B \cdot d\rho_{xy}/dB$ (upper panel) ($\gamma = 0.04$) and Landau index fan diagram (lower panel) as a function of B^{-1} at $T = 50$ mK with B applied in z . (F) ρ_{xx} and (G) ρ_{xy} as a function of B for various temperatures $4 \text{ K} \geq T \geq 50 \text{ mK}$ with B applied in z .

Supplementary Materials for

Observation of a three-dimensional fractional quantum Hall response in HfTe₅

S. Galeski, X. Zhao, R. Wawrzyńczak, T. Meng, T. Förster, S. Honnali, N. Lamba, T. Ehmcke, A. Markou, W. Zhu, J. Wosnitza, C. Felser, G. F. Chen and J. Gooth

This PDF file includes:

Materials and Methods

Figs. S1 to S14

Table S1

Materials and Methods

Single crystal sample growth and pre-characterization

Single-crystals of HfTe₅ were obtained via a chemical vapor transport method. Stoichiometric amounts of Hf (powder, 3N) and Te (powder, 5N) were sealed in a quartz ampoule with iodine (7mg/ml) and placed in a two-zone furnace. A typical temperature gradient from 500 °C to 400 °C was applied. After one-month, long ribbon-shaped single crystals were obtained. The typical size of the measured HfTe₅ single crystals is 1 mm × 0.5 mm × 3 mm (width × height × length).

The samples used in this work are of the same batch as the ones reported in Ref. (1) and (2) and have similar Fermi level positions. As shown in these two papers, in our HfTe₅ samples a three-dimensional topological Dirac semimetal state emerges only at around $T_p \approx 65$ K (at which the resistivity shows a pronounced peak), manifested by a large negative magnetoresistance. This Dirac semimetal state marks a phase transition between two distinct weak ($T > T_p$) and strong topological insulator phases ($T < T_p$). At high temperatures the extracted band gap is around 30 meV (185 K), and at low temperatures 10 meV (15 K).(2) However, we note that the Fermi level at these temperatures is not located in the gap, but several meV in the valance band for $T > T_p$ and in the conduction band for $T < T_p$. Hence, our HfTe₅ samples are metallic at high and low temperatures.

Electrical Transport Measurements

Electrical contacts to the HfTe₅ single crystals were defined with an Al hard mask. Ar sputter etching was performed to clean the sample surface prior to the sputter deposition of Ti (20 nm) and Pt (200 nm) with a BESTEC UHV sputtering system. Subsequently, Pt wires were glued to the sputtered pads using silver paint. All electrical transport measurements up to ± 9 T were performed in a temperature-variable cryostat (PPMS Dynacool, Quantum Design), equipped with a dilution refrigerator inset. To avoid contact-resistance effects, only four-terminal measurements were carried out. The longitudinal ρ_{xx} and Hall resistivity ρ_{xy} were measured in a Hall-bar geometry with standard lock-in technique (Zurich instruments MFLI and Stanford

Research SR830), applying a current of 10 μA with a frequency of $f \sim 1$ kHz across a 10 k Ω shunt resistor. The electrical current was always applied along the a -axis of the crystal.

The pulsed magnetic field experiments up to 70 T were carried out at the Dresden High Magnetic Field Laboratory (HLD) at HZDR, a member of the European Magnetic Field Laboratory (EMFL).

Charge-carrier density and mobility from Hall measurements

From linear fits of the low-field Hall measurements (Fig. S2A), we have obtained the temperature-dependent dominant charge-carrier concentration $n = (d\rho_{xy}/d|B| \cdot e)^{-1}$ (Fig. S2B) and the average mobility $\mu = (\rho_{xx,0} en)^{-1}$ (Fig. S2C) of HfTe₅, using a single-band model.

Mapping of the Fermi surface by analyzing Shubnikov-de Haas oscillations

We mapped the Fermi surface of our HfTe₅ samples by analyzing Shubnikov-de Haas oscillations in the temperature (T)-dependent longitudinal magneto-electrical resistivity $\rho_{xx}(\mathbf{B})$.⁽³⁾ In these measurements, the electrical current is applied along the x -axis with the magnetic field set along the x , y , and z directions. The results of our analysis are summarized in Table S1. For all directions, we observe single frequencies $B_{F,i}$, as shown in Fig. 1, Fig. S4, and Fig. S5, with i being the direction of applied magnetic field. The filling factor ν is related to the Fermi surface as $2\pi(\nu + g) = B_{F,i}/B$, where the phase shift g is approximately zero for all samples. From the slope of linear fits in Landau-index fan diagrams, we extract $B_{F,i}$ and use the Onsager relation $B_{F,i} = (\hbar/2\pi e)S_{F,i}$ to extract the Fermi surface cross-section $S_{F,i}$. Here, \hbar is the reduced Planck constant and e is the electron charge. Under the assumption of an ellipsoidal Fermi surface, the Fermi wave vectors are then given by $k_{F,x} = \sqrt{S_{F,y}S_{F,z}}/\sqrt{\pi S_{F,x}}$, $k_{F,y} = \sqrt{S_{F,x}S_{F,z}}/\sqrt{\pi S_{F,y}}$ and $k_{F,z} = \sqrt{S_{F,x}S_{F,y}}/\sqrt{\pi S_{F,z}}$. The $k_{F,i}$ relate then directly to the Fermi wave length $\lambda_{F,i} = 2\pi/k_{F,i}$.

The resistance amplitude of the maxima in the Shubnikov-de Haas oscillations in $\Delta\rho_{xx}(\mathbf{B})$ is proportional to $\chi(\mathbf{B})/\sinh[\chi(\mathbf{B})] \cdot \exp(\omega_c \tau/B)$ with the cyclotron frequency $\omega_c = \frac{e|B|}{m_c}$ and $\chi(\mathbf{B}) = \frac{2\pi^2 k_B T m_c}{\hbar e |B|}$, where m_c is the cyclotron mass. Hence, when plotting $\chi(\mathbf{B})/\sinh[\chi(\mathbf{B})]$ against $1/B$, the carrier lifetime τ can be extracted from the slope of the logarithmic (Fig. S10C-E). The corresponding effective mass can be extracted from fitting the T -dependence to $\chi(\mathbf{B})/\sinh[\chi(\mathbf{B})]$ (Fig. S10F-H). Assuming that the massive Dirac band exhibits a linear dispersion at low energies, we finally can obtain the effective masses m^* from the cyclotron masses in the x , y and z direction: $m_{c,x} = \sqrt{m_y^* m_z^*}$, $m_{c,y} = \sqrt{m_x^* m_z^*}$ and $m_{c,z} = \sqrt{m_y^* m_x^*}$, respectively. The Fermi velocities $v_{F,i}$ can be further obtained with $v_{F,i} m_i^* = \hbar k_{F,i}$. Eventually, the average Fermi energy can be estimated using $E_F = (v_{F,x}^2 \hbar^2 k_{F,x}^2 + v_{F,y}^2 \hbar^2 k_{F,y}^2 + v_{F,z}^2 \hbar^2 k_{F,z}^2)^{0.5}$. For sample A we obtain $E_F = (9 \pm 2)$ meV, where the deviation is obtained from the error of the fits in $k_{F,i}$ and $v_{F,i}$.

Comment on the calculation of the Hall conductivity tensor element

We calculate the Hall conductivity tensor element σ_{xy} using $\sigma_{xy} = \rho_{xy}/(\rho_{xx}^2 + \rho_{xy}^2)$, assuming that $\rho_{xx} = \rho_{yy}$. However, in general $\sigma_{xy} = \rho_{xy}/(\rho_{xx}\rho_{yy} + \rho_{xy}^2)$ with a magnetic field in z -direction. Due to the geometry of the HfTe₅ crystals (elongated needles) and its mechanical fragility, performing reliable measurements of ρ_{yy} on our samples is not possible. Instead, we estimate the error of the σ_{xy} using the ratio of Drude resistivities $\rho_{yy}/\rho_{xx} = (n_{xy}e^2\tau_x/m_x^*)/(n_{xy}e^2\tau_y/m_y^*)$ estimated from the quantum lifetimes and effective masses obtained from Shubnikov-de Haas oscillations on sample A, given in Supplementary Table 1. n_{xy} is the charge-carrier concentration in the x - y -plane. Based on this analysis we find $\rho_{yy}/\rho_{xx} \approx 0.4$, which results in an error of 2 % in the estimated σ_{xy} at the 3/5 plateau and in an error of 8 % in the estimated σ_{xy} at the 6/5 plateau, owing to $\rho_{xx}(\mathbf{B}) < \rho_{xy}(\mathbf{B})$. Both these errors lay well within the estimated error of $k_{F,z}$ of 10 %. Therefore, the fractional filling factors of the Hall plateaus in ρ_{xy} are expected to be observable in the Hall plateaus in σ_{xy} .

Theory of the three-dimensional Hall effect

Hall effect stacks in momentum space

Two-dimensional electrons subject to a magnetic field \mathbf{B} form Landau levels of energy $E_N = (N + \frac{1}{2})\hbar\omega_c$, where $N = \nu - 1$ is the Landau level index with the filling factor ν . A three-dimensional Hall system can be understood as stacking of such two-dimensional Hall layers on top of each other. Any finite hopping along the third direction - here taken to be the direction of the magnetic field: the z -direction - results in an additional dispersion with the momentum p_z along z . The Landau levels consequently form bands of energy $E_N(p_z) = (N + \frac{1}{2})\hbar\omega_c + \frac{p_z^2}{2m_z^*}$, where m_z^* is the mass associated with the z -dispersion, and it is more convenient to think about a 3D Hall system in momentum space. If the energy $E_N(p_z)$ of a given band N is below the Fermi level E_F for a certain momentum range $\Delta p_{z,N}$ (see Fig. S4), then the corresponding 2D-momentum layers (layers of p_x and p_y) are occupied and gapped. Their gap $\Delta_N(p_z)$ is the energy difference of these states to the Fermi level, $\Delta_N(p_z) = E_F - E_N(p_z)$. Each of the occupied momentum-space layers carries one quantum of Hall conductance.

As shown in Fig. S5, the density of states of a 3D Hall system is that of a macroscopically degenerate sets of one-dimensional bands: van-Hove singularities at the band bottoms are followed by tails extending to high energies. The degeneracy of these bands equals the macroscopic degeneracy $J_{LL} = \frac{e|\mathbf{B}|}{2\pi\hbar} L_x L_y$ of individual Landau levels, where L_i is the length of the system along the i -direction. The total density of states of a 3D Hall system without additional gaps is thus generally finite at the Fermi level, reflecting the fact that the Fermi level intersects Landau level bands.

In an ideal model system, each occupied 2D-momentum layer contributes one quantum of Hall conductance $\frac{e^2}{h}$, giving rise to a total 3D Hall conductivity of $\sigma_{xy} = \sum_N \frac{\Delta p_{z,N}}{2\pi\hbar} \frac{e^2}{h}$. This does, however, not mean that the 3D Hall conductivity is quantized in real samples. First, given that there are gapless bulk states at the Fermi level, disorder-induced couplings of the edge states across the sample can destroy the quantization of the Hall response. Secondly, any small change of the E_F changes $\Delta p_{z,N}$, and thus also σ_{xy} , in some non-universal way. The gapless bulk states

also give rise to a finite, non-universal longitudinal conductivity. A truly quantized Hall response can only arise when an additional gap opens at the Fermi level.(4) Consider the example that the chemical potential resides in the lowest Landau level. If the system then forms a density wave with wave vector $G_z = \Delta p_{z,0}/\hbar$, the spectrum is fully gapped, the Hall conductivity is quantized to $\sigma_{xy} = \frac{G_z e^2}{2\pi h}$, and the longitudinal conductivity vanishes.

Fixed chemical potential vs. fixed particle number

The electric response of a Hall sample can take qualitatively different forms depending on whether an experiment is performed at fixed particle number or at fixed chemical potential, *i.e.* Fermi level.

(i) Fixed chemical potential

If a small sample is strongly connected to large reservoirs, these fix the chemical potential in the sample. Given that the Landau level bands move with magnetic field and because their degeneracy increases linearly with field, a fixed chemical potential implies a varying total electron density n_{tot} . Whenever a Landau-level band bottom crosses the chemical potential, its van Hove singularity induces a kink in the density of electrons in the sample. The Hall response likewise features kinks when a Landau level crosses the chemical potential. These kinks are followed by a plateau-like feature. The longitudinal resistivity depends on the bulk density of states at the Fermi level, and therefore exhibits spikes whenever a Landau-level band bottom crosses E_F . To illustrate this behavior, we extend the treatment of the 2D quantum Hall effect presented in Ref. (5) to three dimensions by including a dispersion of the Landau-level bands and summing over all p_z . Following Ref. (5), we keep track of a Lorentzian level broadening, and also introduce a transport lifetime τ_M (in contrast to the quantum lifetime encoding how long it takes an electron to be scattered into any other state, the transport lifetime encodes that forward scattering does not alter transport). As Ref. (5), we choose the transport lifetime to be ten times larger than the quantum lifetime, which in turn is defined by the inverse level broadening. The resulting electron density, Hall conductivity, and longitudinal resistivity are shown in Fig. S6A-C. The quantum limit is reached when the $N = 1$ -Landau level band has shifted above the chemical potential such that only states in the $N = 0$ Landau-level band are occupied. In Fig. S6A-C, the quantum limit approximately corresponds to $3 \text{ T} < |\mathbf{B}| < 9 \text{ T}$. Above 9 T, also the zeroth Landau-level shifts above the chemical potential (its low-energy tail results in a small residual electron density that disappears when $|\mathbf{B}|$ increases further).

(ii) Fixed particle number

In samples containing many electrons, a change of the electron density costs a large charging energy.(6) If such a large sample is only weakly coupled to leads, the particle number rather than the chemical potential is kept fixed when the magnetic field is varied. This in turn requires the chemical potential to vary as a function of magnetic field. Each time a Landau-level bottom crosses the varying chemical potential, the chemical potential exhibits a peak. Using that the Landau-level degeneracy is given by J_{LL} , one furthermore finds that the Hall conductivity is given by $\sigma_{xy} = \frac{e^2}{h} \frac{2\pi \hbar}{e B} n_{tot}$: The

Hall conductivity exhibits a featureless $1/|\mathbf{B}|$ -behaviour. In contrast, the van Hove singularities associated with Landau-level band bottoms still induce spikes in the longitudinal conductivity. This behavior of a 3D Hall sample at fixed particle number is illustrated in Fig. S6D-F.

(iii) Role of level broadening

In a system with fixed particle number, the inclusion of level broadening smoothens out the dependence of the chemical potential on the magnetic field. As a result, the Hall response is slightly closer to the Hall response of a system with fixed chemical potential: we find that the Hall conductivity exhibits small kinks once level broadening is considered.

(iv) Specifics of our samples

In general, a real sample will be in between the two extreme cases of fixed conduction electron (charge carrier) number and fixed chemical potential (Fermi level). This is also apparent from the behavior our samples. At small fields, the Hall response shows slightly smoothed kinks, followed by plateau-like features. This behavior is similar to the theoretical expectations for a system at fixed chemical potential. We note that our samples are not very large, and that the Dirac pocket is comparably small. Furthermore, at magnetic fields below the quantum limit, the variation of particle density in our toy model at exactly fixed chemical potential is at most about 20%. Finally, the chemical potential does not have to be perfectly conserved for the Hall data to exhibit kinks and plateau-like features: an ideal $1/|\mathbf{B}|$ -behavior arises only if the chemical potential adjusts perfectly, and if the level broadening is small. Our data, therefore, suggests the presence of localized states that can soak up/release some amount of conduction electrons in order to keep the chemical potential of the sample closer to the chemical potential in the leads. At fields beyond the quantum limit and temperatures at which the $\nu = 3/5$ -plateau has not yet developed, the Hall conductivity instead follows a $1/|\mathbf{B}|$ -behavior. We interpret this behavior as the system's tendency to avoid large changes of the conduction electron density. Finally, the electrons in our samples form a (gapped) Dirac semimetal rather than a quadratic dispersion. As a consequence, the spectrum is particle-hole symmetric. If the Zeemann effect is negligible, all Landau levels except for the zeroth Landau levels above and below the node are spin-degenerate (the zeroth Landau levels are non-degenerate). The levels with $|N| > 0$ shift in field, while the zeroth Landau levels are unaffected by the field. With Zeeman splitting, the $|N| > 0$ Landau levels are Zeeman-split and the $N = 0$ -Landau levels shift in field. We find that the main difference between a Dirac semimetal and 3D electrons with a quadratic dispersion is the precise location of the various plateaus, but that the main features are qualitatively identical. Most importantly, because the zeroth Landau levels of a Dirac semimetal shift only very weakly at small fields, even when the Zeeman is effect included, the range of occupied momenta in the $N = 0$ -band is $\Delta p_{z,0}(B) \approx \Delta p_{z,0}(B = 0) = 2\hbar k_{F,z}$. As a result, the Hall conductivity just above the quantum limit is given by $\sigma_{xy} = \frac{\Delta p_{z,0}}{2\pi\hbar} \frac{e^2}{h} \approx \frac{2k_{F,z}}{2\pi} \frac{e^2}{h}$. Only at larger fields, when the chemical potential is renormalized substantially, does the Hall conductivity drop.

In contrast to 2D quantum Hall systems, the interplay of the different temperature-dependencies of the finite values of ρ_{xx} at its minima and the metal-insulator transition at high fields in HfTe₅, cause the position of the minima in $\rho_{xx}(\mathbf{B})$ to shift in temperature

(Fig 3F). However, importantly, we note that below 800 mK, the positions of the minima up to 5 T remain at fixed positions in magnetic field for all temperatures. This enables the assignment of filling factors to the minima of $\rho_{xx}(\mathbf{B})$ up to that field in this low-temperature range.

Supplementary Figures

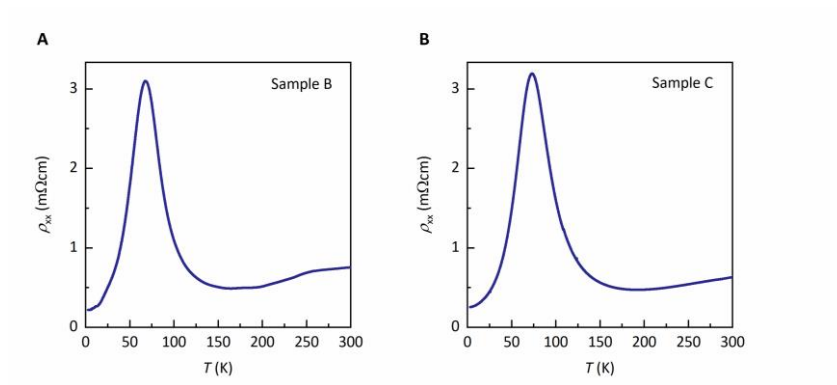


Fig. S1. Longitudinal resistivity ρ_{xx} of HfTe₅ sample B and C as a function of temperature T at zero magnetic field. (A) ρ_{xx} of sample B and (B) ρ_{xx} of sample C.

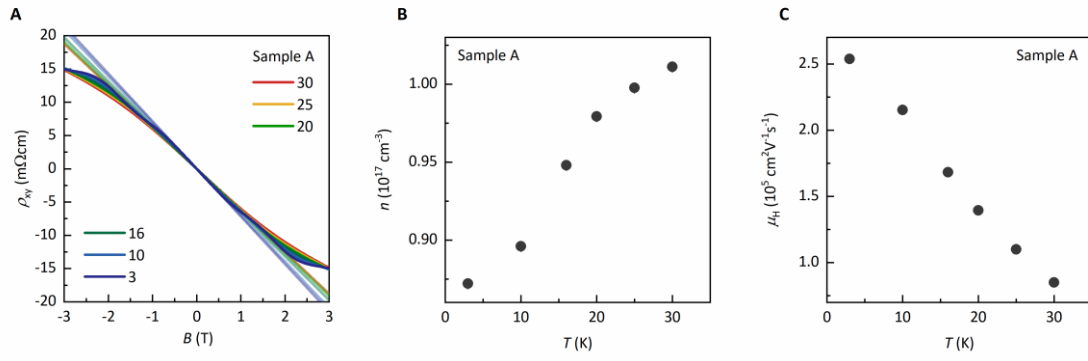


Fig. S2. Charge-carrier concentration and Hall mobility of sample A. (A) Linear fits of the Hall resistivity at low magnetic fields (fit range ± 0.5 T). (B) Extracted charge-carrier concentration $n = (d\rho_{xy}/d|B| \cdot e)^{-1}$ from the slope of the linear fits $d\rho_{xy}/d|B|$. Here, e is the electron charge. (C) Calculated Hall mobility $\mu_H = (\rho_{xx} \cdot e \cdot n)^{-1}$.

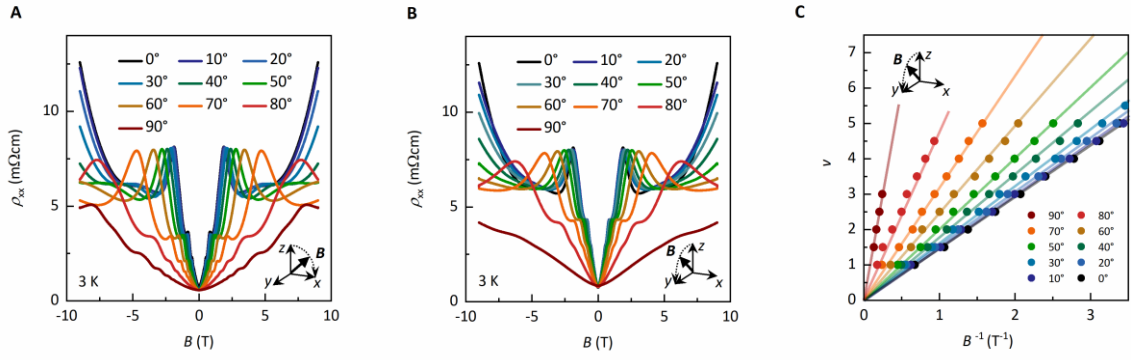


Fig. S3. Rotation angle-dependence of the Shubnikov-de Haas oscillations. (A) ρ_{xx} versus B for various rotation angles of B in the z - x plane and (B) ρ_{xx} in the y - x plane at 3 K. (C) Landau-level fan diagram for various rotation angles of B in the y - x plane at 3 K. The data is obtained from the minima of ρ_{xx} in B.

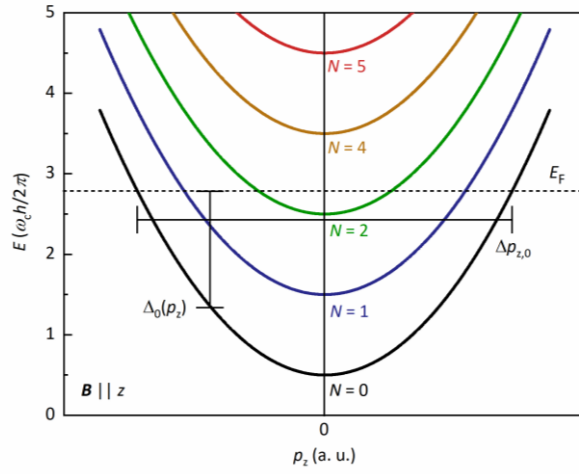


Fig. S4. Landau-level band structure of a 3D Hall system. Energy E as a function of momentum p_z for a magnetic field \mathbf{B} applied in z -direction. The Landau levels are indexed as indices $N = \nu + 1$. E_F denotes the Fermi level. $\Delta p_{z,0}$ is the distance between the momentum points of the $N = 0$ Landau level at E_F . $\Delta_0(p_z)$ is the energy difference of the states of the $N = 0$ Landau level and E_F .

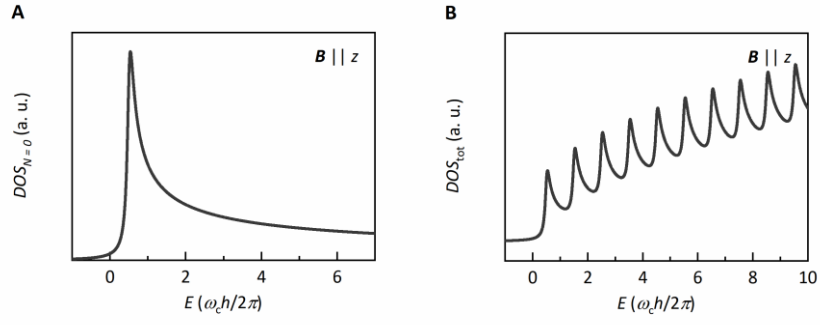


Fig. S5. Density of states of Landau-level bands. (A) Density of states $DOS_{N=0}$ of the $N=0$ Landau level and (B) total density of states $DOS_{\text{tot}} = \sum_N DOS_N$ of a 3D Hall system as a function of energy E . DOS_N is the density of states of the N th Landau level. To mimic the effects of disorder, we have included a Lorentzian level broadening for the Landau levels, which smoothens out the van Hove singularities at the band bottoms.

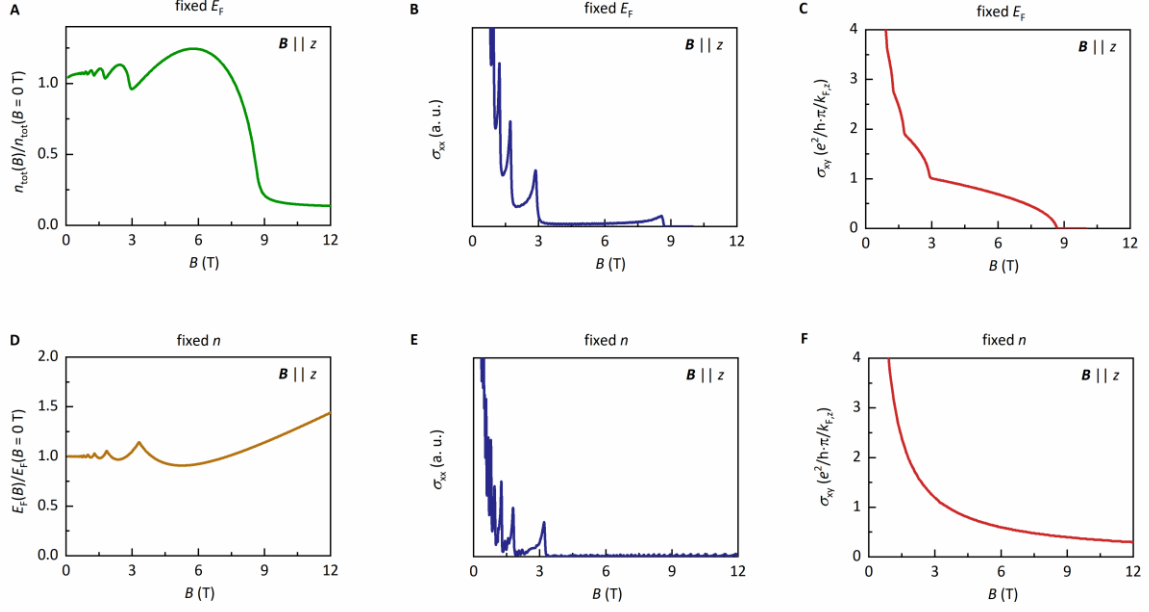


Fig. S6. 3D Hall effect at fixed Fermi energy E_F and at fixed particle number n . (A) Relative electron number, (B) longitudinal conductivity σ_{xx} and (C) Hall conductivity σ_{xy} normalized by the zero field Fermi wavevector k_{Fz} as a function of magnetic field \mathbf{B} in z -direction for fixed E_F . In the calculations, we exemplarily choose the band mass $m = m^* = 0.067 m_e$, where m_e is the free-electron mass, the Fermi level 7.5 meV, and the Landau-level broadening 0.12 meV. (D) Relative Fermi level, (E) σ_{xx} , and (F) σ_{xy} as a function of \mathbf{B} in z -direction for fixed n . The same model parameters and zero-field electron density as for the calculations with fixed E_F were used, except for the level broadening and the transport lifetime, which were both divided by a factor of 10 in this case.

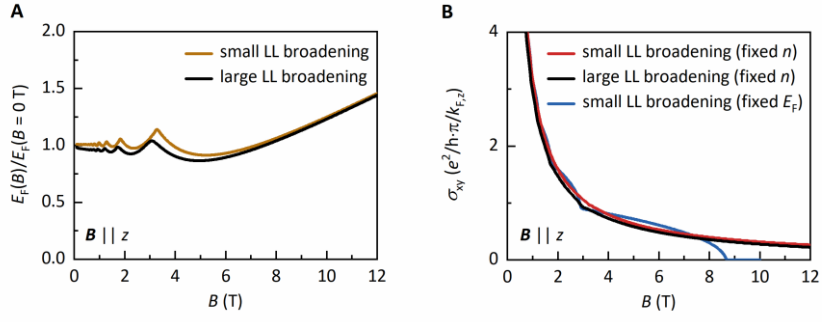


Fig. S7. 3D Hall effect at fixed particle number for a larger level broadening (A) Relative Fermi level and **(B)** Hall conductivity σ_{xy} normalized by the zero field Fermi wavevector k_{Fz} as a function of magnetic field B in z -direction. The yellow and red solid curves correspond to the same model parameters and zero-field electron density as in Fig. S6 D and F, respectively (small Landau level broadening and transport lifetime). The black curves use ten times larger level broadening and transport lifetime. For comparison, panel B also shows the Hall conductivity at fixed Fermi level from Fig. S6 C (blue curve).

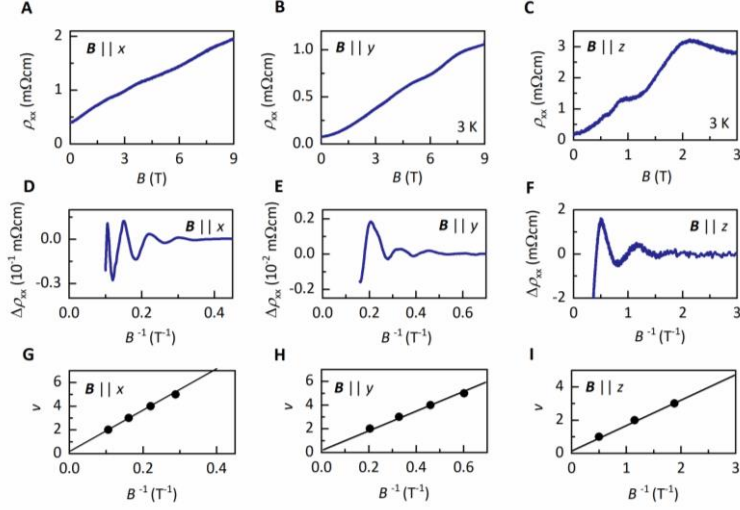


Fig. S8. Analysis of the Shubnikov-de Haas oscillations of sample B at 3 K with the magnetic field applied along the three principal axes x , y , and z . (A) ρ_{xx} as a function of B at 3 K with B applied along x , (B) along y and (C) along the z -direction. (D) Variation of the longitudinal electrical resistivity $\Delta\rho_{xx}$ as a function of B at 3 K with B applied along x , (E) along y and (F) along the z -direction. (G) Landau-index fan diagram for the integer filling factors ν with B applied along x , (H) along y , and (I) along the z -direction.

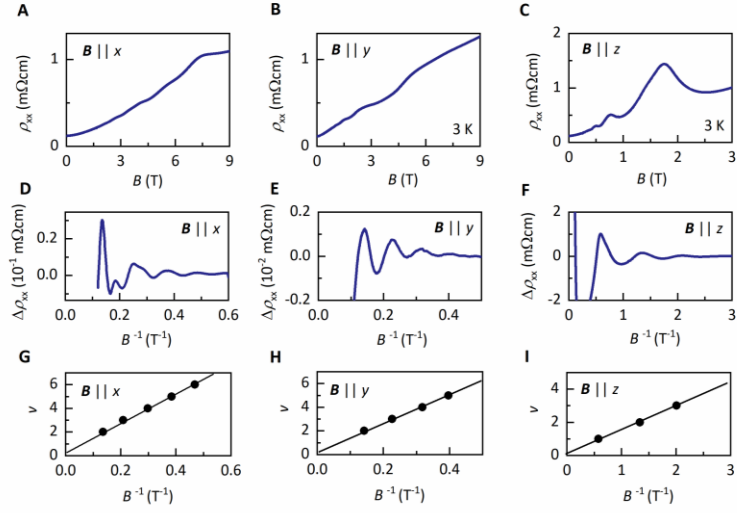


Fig. S9. Analysis of the Shubnikov-de Haas oscillations of sample C at 3 K with the magnetic field applied along the three principal axes x , y , and z . (A) ρ_{xx} as a function of B at 3 K with B applied along x , (B) along y and (C) along the z -direction. (D) Variation of the longitudinal electrical resistivity $\Delta\rho_{xx}$ as a function of B at 3 K with B applied along x , (E) along y , and (F) along the z -direction. (G) Landau-index fan diagram for the integer filling factors ν with B applied along x , (H) along y , and (I) along the z -direction.

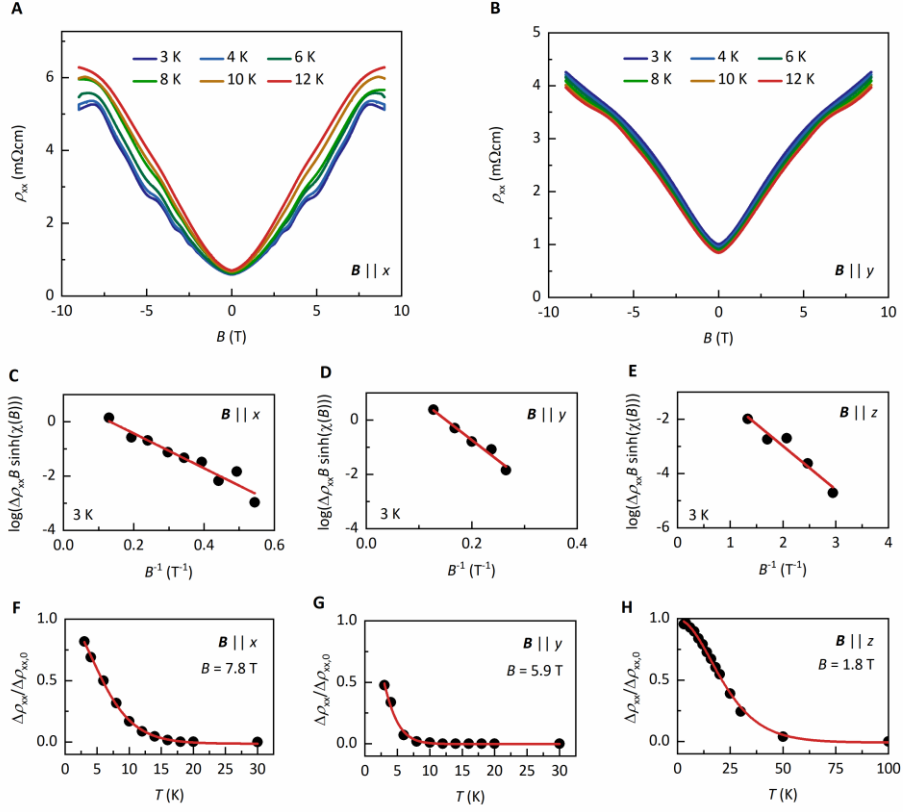


Fig. S10. Determination of the mobility and cyclotron mass. (A) ρ_{xx} as a function of B for various temperatures $T \geq 3$ K with B applied in x and (B) in y . (C) Dingle plots of $\Delta\rho_{xx}|B/\sinh[\chi(T)]$ versus B^{-1} with $\chi(B) = \frac{2\pi^2 k_B T m_c}{\hbar e B}$ at 3 K with B applied along x , (D) along y and (E) along the z -direction. The lines are linear fits to the measurement data to obtain the electron mobility μ , as explained in Materials and Methods. (F) The cyclotron masses m_c for B applied along x , (G) along y and (H) along the z -direction is obtained from fits (red lines) to $\Delta\rho_{xx}/\Delta\rho_{xx,0}$, where $\Delta\rho_{xx,0}$ is the extrapolated $\Delta\rho_{xx}$ at zero Kelvin. $\Delta\rho_{xx}$ for each principal direction is taken at the magnetic field of the lowest accessible Landau level.

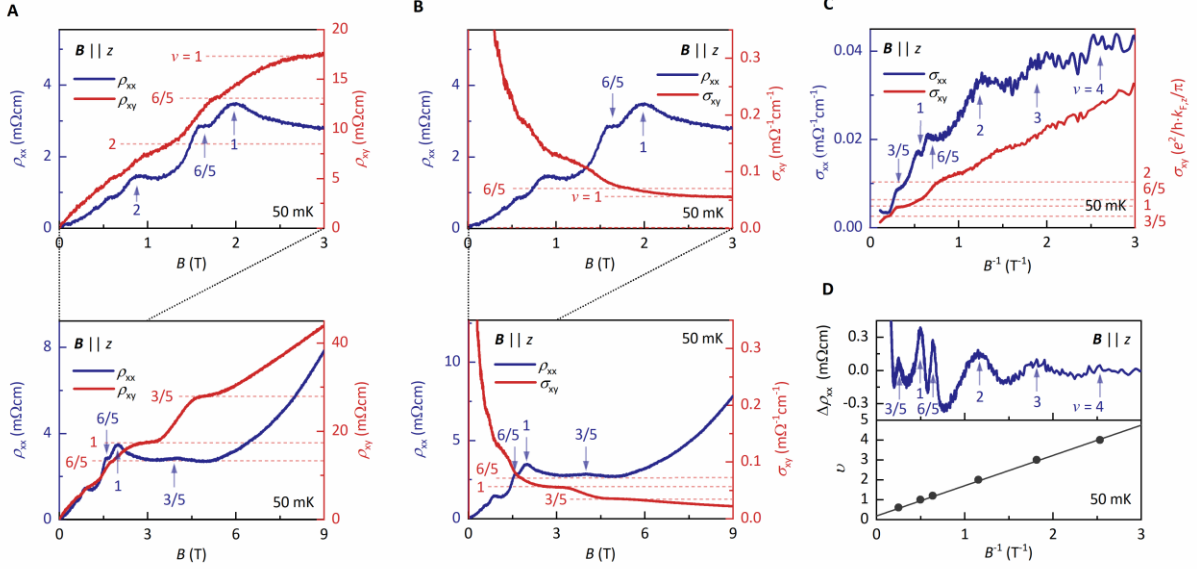


Fig. S11. Three-dimensional fractional quantum Hall effect in sample B. (A) Longitudinal electrical resistivity ρ_{xx} (blue, left axis) and Hall resistivity ρ_{xy} (red, right axis) as a function of B at $T = 50$ mK with B applied in z for $0 \text{ T} \leq B \leq 3 \text{ T}$ (upper panel) and $0 \text{ T} \leq B \leq 9 \text{ T}$ (lower panel). The blue arrows mark the onset of a Landau level (LL). The blue and red numbers label the filling factor ν of the corresponding LL. (B) Longitudinal electrical resistivity ρ_{xx} (blue, left axis) and Hall conductivity σ_{xy} (red, right axis) as a function of B at $T = 50$ mK with B applied in z for $0 \text{ T} \leq B \leq 3 \text{ T}$ (upper panel) and $0 \text{ T} \leq B \leq 9 \text{ T}$ (lower panel). (C) Longitudinal electrical conductivity σ_{xx} (blue, left axis) and Hall conductivity σ_{xy} (red, right axis) as a function of B^{-1} at $T = 50$ mK with B applied in z . (D) Variation of the longitudinal electrical resistivity $\Delta\rho_{xx}$ as a function of B at 50 mK with B applied along z (upper panel) and Landau-index fan diagram (lower panel) as a function of B^{-1} at $T = 50$ mK with B applied in z .

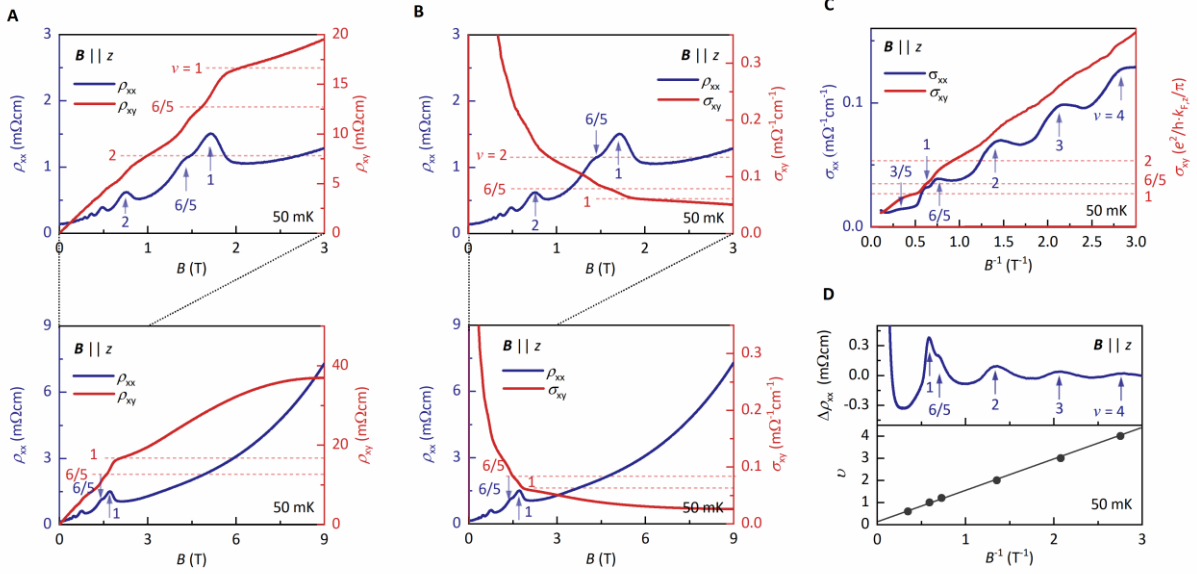


Fig. S12. Three-dimensional fractional quantum Hall effect in sample C. (A) Longitudinal electrical resistivity ρ_{xx} (blue, left axis) and Hall resistivity ρ_{xy} (red, right axis) as a function of \mathbf{B} at $T = 50$ mK with \mathbf{B} applied in z for $0 \text{ T} \leq \mathbf{B} \leq 3 \text{ T}$ (upper panel) and $0 \text{ T} \leq \mathbf{B} \leq 9 \text{ T}$ (lower panel). The blue arrows mark the onset of a Landau level (LL). The blue and red numbers label the filling factor ν of the corresponding LL. (B) Longitudinal electrical resistivity ρ_{xx} (blue, left axis) and Hall conductivity σ_{xy} (red, right axis) as a function of \mathbf{B} at $T = 50$ mK with \mathbf{B} applied in z for $0 \text{ T} \leq \mathbf{B} \leq 3 \text{ T}$ (upper panel) and $0 \text{ T} \leq \mathbf{B} \leq 9 \text{ T}$ (lower panel). (C) Longitudinal electrical conductivity σ_{xx} (blue, left axis) and Hall conductivity σ_{xy} (red, right axis) as a function of \mathbf{B}^{-1} at $T = 50$ mK with \mathbf{B} applied in z . (D) Variation of the longitudinal electrical resistivity $\Delta\rho_{xx}$ as a function of \mathbf{B} at 50 mK with \mathbf{B} applied along z (upper panel) and Landau-index fan diagram (lower panel) as a function of \mathbf{B}^{-1} at $T = 50$ mK with \mathbf{B} applied in z .

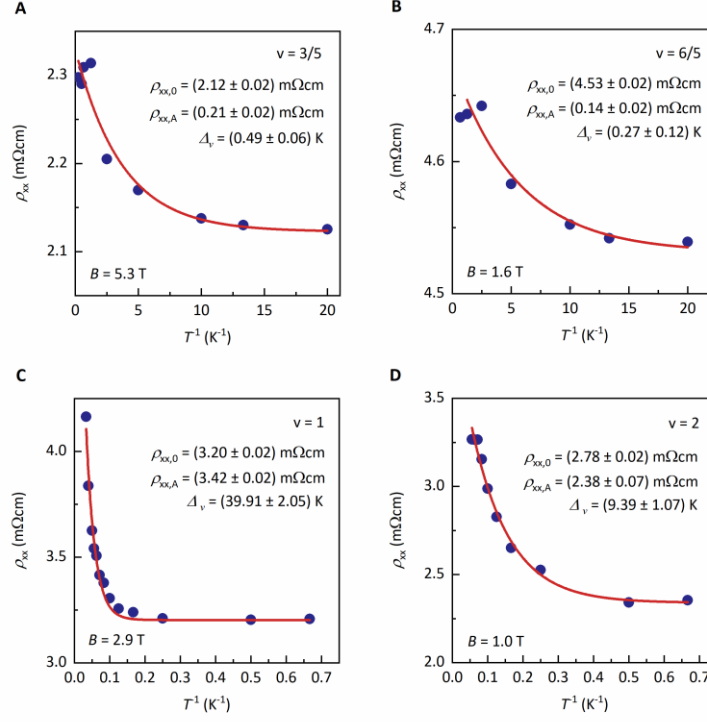


Fig. S13. Fit of the gap energies. (A) ρ_{xx} as a function of T^{-1} at the magnetic field B of the Shubnikov-de Haas minima of filling factor $\nu = 3/5$, (B) $\nu = 6/5$, (C) $\nu = 1$, (D) $\nu = 2$. The gap energies Δ_ν are fitted (red lines) in the thermally activated regime $\rho_{xx}(B_z) = \rho_{xx,A} \exp(\Delta_\nu/2k_B T) + \rho_{xx,0}$, where k_B is the Boltzmann constant, $\rho_{xx,A}$ a scaling factor and $\rho_{xx,0}$ accounts for the finite ρ_{xx} in the Shubnikov-de Haas minima due to disorder broadening of the Landau levels.

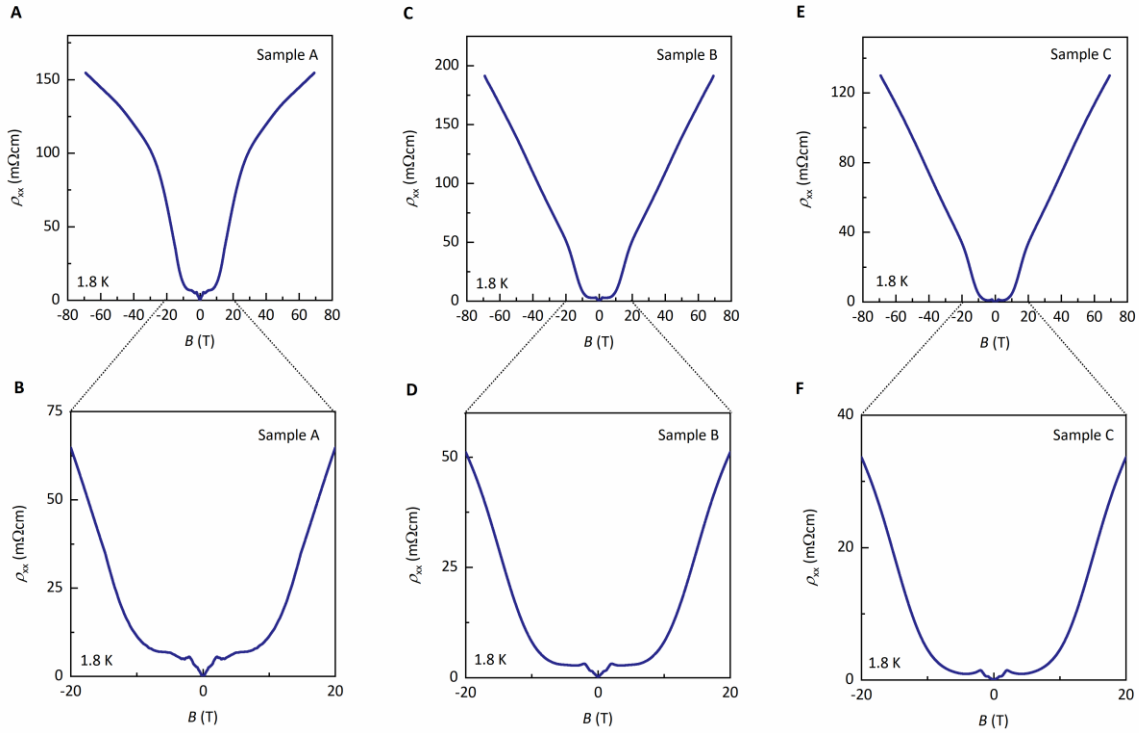


Fig. S14. High-field magneto-transport. (A) Longitudinal electrical resistivity ρ_{xx} of sample A at 1.8 K as a function of magnetic field $\mathbf{B} \parallel z$ up to ± 70 T and (B) up to ± 20 T. (C) ρ_{xx} of sample B at 1.8 K as a function of \mathbf{B} up to ± 70 T and (D) up to ± 20 T. (E) ρ_{xx} of sample C at 1.8 K as a function of \mathbf{B} up to ± 70 T and (F) up to ± 20 T. For all samples investigated, no additional local maxima are observed above 9 T.

Supplementary Tables

Sample	Magnetic field's direction	SdH frequency	Fermi area	Fermi wave vector	Fermi wave length	Cyclotron mass	Effective mass	Fermi velocity	Dingle temperature	Lifetime
		B_F (T)	S_F (10^{-4} \AA^{-2})	k_F (10^{-3} \AA^{-1})	λ_F (nm)	m_c (m_0)	m^* (m_0)	v_F (10^5 m/s)	T_D (K)	τ (ps)
A	$\mathbf{B} \parallel x$	9.9 ± 0.1	9.9 ± 0.1	5.2 ± 0.9	120 ± 23	0.117 ± 0.002	0.034 ± 0.001	1.8 ± 0.5	0.17 ± 0.02	0.11 ± 0.01
	$\mathbf{B} \parallel y$	14.5 ± 0.2	14.5 ± 0.2	7.7 ± 1.5	82 ± 15	0.303 ± 0.019	0.005 ± 0.001	17.5 ± 3.5	0.07 ± 0.01	0.05 ± 0.01
	$\mathbf{B} \parallel z$	1.3 ± 0.1	1.3 ± 0.1	57.7 ± 5.9	11 ± 1	0.117 ± 0.002	2.714 ± 0.253	0.2 ± 0.1	0.69 ± 0.1	0.45 ± 0.06
B	$\mathbf{B} \parallel x$	8.4 ± 0.1	8.4 ± 0.1	5.3 ± 0.6	-	-	-	-	-	-
	$\mathbf{B} \parallel y$	12.9 ± 0.6	12.9 ± 0.6	8.2 ± 2.2	-	-	-	-	-	-
	$\mathbf{B} \parallel z$	1.4 ± 0.1	1.4 ± 0.1	48.3 ± 8.9	13 ± 2	-	-	-	-	-
C	$\mathbf{B} \parallel x$	8.8 ± 0.1	8.8 ± 0.1	5.9 ± 0.2	-	-	-	-	-	-
	$\mathbf{B} \parallel y$	10.5 ± 1.2	10.5 ± 1.2	7.0 ± 3.2	-	-	-	-	-	-
	$\mathbf{B} \parallel z$	1.3 ± 0.2	1.3 ± 0.2	47.6 ± 1.5	13 ± 2	-	-	-	-	-

Table S1. Band-structure parameters of HfTe₅ sample A, B, and C, obtained from Shubnikov-de Haas oscillations. The variations denote the errors from the fits and from error propagation as explained in the methods and main text.

Supplementary References

1. L.-X. Zhao, X.-C. Huang, Y.-J. Long, D. Chen, H. Liang, Z.-H. Yang, M.-Q. Xue, Z.-A. Ren, H.-M. Weng, Z. Fang, Anomalous magneto-transport behavior in transition metal pentatelluride HfTe₅. *Chinese Phys. Lett.* **34**, 37102 (2017).
2. Y. Zhang, C. Wang, G. Liu, A. Liang, L. Zhao, J. Huang, Q. Gao, B. Shen, J. Liu, C. Hu, Temperature-induced Lifshitz transition in topological insulator candidate HfTe₅. *Sci. Bull.* **62**, 950–956 (2017).
3. F. Tang, Y. Ren, P. Wang, R. Zhong, J. Schneeloch, S. A. Yang, K. Yang, P. A. Lee, G. Gu, Z. Qiao, L. Zhang, Three-dimensional quantum Hall effect and metal–insulator transition in ZrTe₅. *Nature.* **569**, 537–541 (2019).
4. B. I. Halperin, Possible states for a three-dimensional electron gas in a strong magnetic field. *Jpn. J. Appl. Phys.* **26**, 1913 (1987).
5. A. Endo, N. Hatano, H. Nakamura, R. Shirasaki, Fundamental relation between longitudinal and transverse conductivities in the quantum Hall system. *J. Phys. Condens. Matter.* **21**, 345803 (2009).
6. G. D. Mahan, *Many-particle physics* (Springer Science & Business Media, 2013).